8

SAR Modes

8.1 Introduction

Most spaceborne synthetic aperture radars (SARs) can be operated in several imaging modes and can have up to four polarizations. Indeed, there can be 10s of possible operating configurations for some SAR missions. Interferometry requires that the reference and repeat images be in the same, or similar, modes and have the same polarization. Here we discuss the possible modes and polarizations using the ALOS-1 mission as an example. We begin this chapter by noting that the swath width of a standard strip-mode SAR is limited by the need to wait for the pulse to sweep across the Earth from the near range to the far range before sending another radar pulse (Figure 8.1). Otherwise, the return signals from the near and far ranges would overlap in time (Box 8.1).

Box 8.1

Review of Constraints on PRF and Swath Width

As discussed in Section 2.4, the single-look azimuth resolution of a SAR is equal to one half the length of the antenna, $L/2$. To achieve this resolution, the pulse repetition frequency PRF of the radar must exceed $2V/L$ where V is the ground velocity of the spacecraft. In Section 3.2 we calculated the ground velocity for a satellite in low Earth orbit. For example, a satellite at an altitude of 700 km has a ground velocity of 6.75 km/s. Increasing the altitude to 1 500 km only reduces the ground velocity to 5.8 km/s. Thus, the lower bound on the PRF is essentially determined by the length of the antenna. For a typical 10-m long antenna, the PRF must exceed 1 200 Hz.

There is also an upper bound on the PRF. Before the SAR can send a new pulse, one must wait until the prior pulse propagates from the near range to the far range (Figure 8.1). Otherwise, the return signals from the near and far ranges would overlap in time. Moreover, as discussed in Section 4.4, to reduce the peak power output of the transmit antenna, the radar sends a frequency-modulated chirp (Figure 4.4). This chirp propagates to the ground where it reflects from a swath typically 70 km wide. When it returns to the radar, the raw signal data consists of the complex reflectivity of the

Downloaded from https://www.cambridge.org/core. UNIVERSIDAD AUTONOMA METROPOLITANA, on 11 Nov 2026 at 05:35:40, subject to the Cambridge Core terms of use, available at https://www.cambridge.org/core/terms. https://doi.org/10.1017/9781009606226.009

surface convolved with the chirp. The chirp is deconvolved in the SAR-processor program. A typical chirp length is 10 km, so this adds roughly 30% to the required wait time. The bounds on the PRF are given by

$$\frac{2V}{L} < \text{PRF} < \frac{c}{2H}(\sec\theta_2 - \sec\theta_1)^{-1}$$

where c is the speed of light and H is the altitude of the spacecraft. The look angles to the near range θ_1 and the far range θ_2 govern the width of the swath. As discussed in Chapter 3, the sweet spot for the altitude of a remote sensing satellite is 700 km. Therefore, the only adjustable parameters on the PRF bounds are the antenna length and the swath width. One could achieve a 350 km wide swath by increasing the antenna length from 10 m to 50 m, although this would add considerable expense to the SAR mission. Also, this would reduce the PRF by a factor of 5, which would result in five times poorer azimuth resolution and thus fewer looks for averaging. Elachi and Van Zyl (2021) discuss these PRF constraints and show that the width of the swath is fundamentally limited by the area of the antenna; a longer or wider antenna is needed to make a wider swath. SweepSAR, discussed later in Section 8.6, increases the swath width by effectively increasing the width of the antenna.

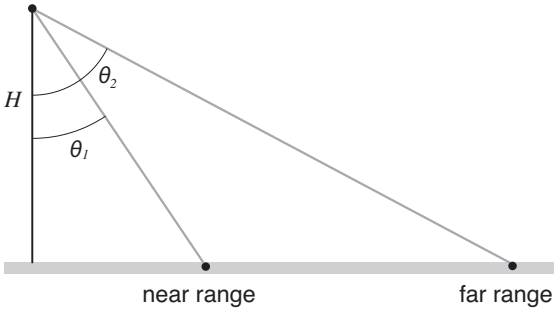


Figure 8.1 End view of the distance to the near range and far range of the radar illumination pattern. For standard strip-mode SAR, there can only be one pulse sweeping across the swath.

A diagram of two main spatial modes for the ALOS-1 PALSAR radar is shown in Figure 8.2. The standard strip mode, discussed in Chapters 2 and 4, has a swath width that is limited by the need to wait for the radar pulse to propagate from the near range to the far range before sending another pulse (Box 8.1). For the ALOS-1 PALSAR configuration, the maximum swath width is 70 km. The ScanSAR mode is used to acquire a wider swath of 350 km from a single acquisition. This ScanSAR configuration has five subswaths each 70 km wide to achieve the overall swath of 350 km (Figure 8.3). The details and limitations of the ScanSAR technique are discussed later in this chapter. As seen in Figure 8.2, there are 18 possible positions

Downloaded from https://www.cambridge.org/core. UNIVERSIDAD AUTONOMA METROPOLITANA, on 11 Nov 2026 at 05:35:40, subject to the Cambridge Core terms of use, available at https://www.cambridge.org/core/terms. https://doi.org/10.1017/9781009606226.009

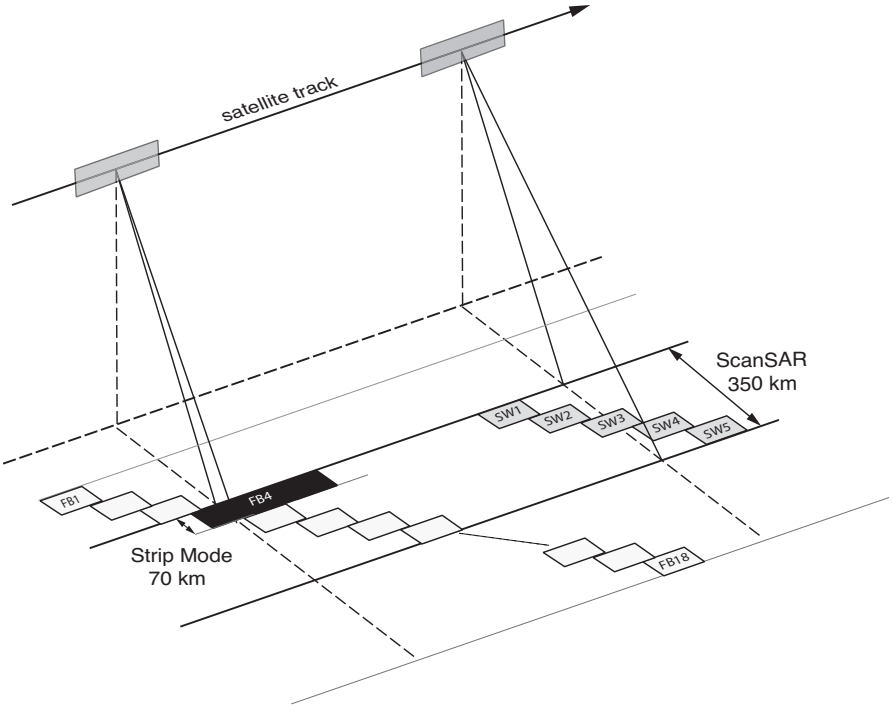


Figure 8.2 The two basic operating modes of the ALOS-1 PALSAR are strip mode and ScanSAR mode. The location of the swath in range is called the beam # and there are 18 possible beams, although only five are commonly used. The commonly used ScanSAR mode has five subswaths matching five of the beams in the swath mode data to achieve a 350 km wide swath.

for the location of the swath in range although in practice only five swath locations were commonly used.

8.2 Polarization

In addition to the cross-track position of swaths, data can be collected in four polarizations (Zebker and Van Zyl, 1991). SAR satellites generally use linearly polarized EM radiation. When the electric field vector is parallel to the ground, this is called horizontal polarization H. There is one polarization for the transmitted waves and a second for the receive waves, so four polarizations are possible:

HH — horizontal transmit, horizontal receive;
HV — horizontal transmit, vertical receive;
VV — vertical transmit, vertical receive; and
VH — vertical transmit, horizontal receive.

Downloaded from https://www.cambridge.org/core. UNIVERSIDAD AUTONOMA METROPOLITANA, on 11 Nov 2026 at 05:35:40, subject to the Cambridge Core terms of use, available at https://www.cambridge.org/core/terms. https://doi.org/10.1017/9781009606226.009

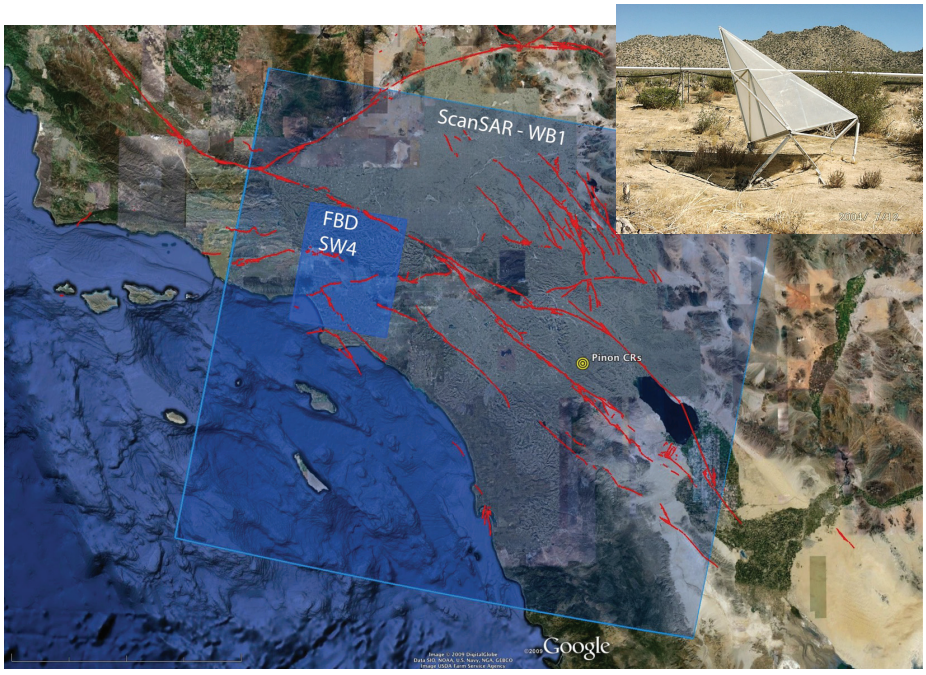


Figure 8.3 Spatial coverage of ALOS-1 strip mode and ScanSAR data. Subswath 4 (SW4) of the ScanSAR overlaps with a strip-mode fine beam dual polarization acquisition, so one can perform ScanSAR to strip-mode interferometry. A Piñon Flat corner reflector is shown in the inset.

The PALSAR was operated in three polarimetric modes (Table 8.1):

1) fine beam single polarization (FBS) (HH) or (VV);
2) fine beam dual polarization (FBD) (HH+HV) or (VV+VH); and
3) quad polarization (PLR) (HH+HV+VV+VH).

8.3 Range and Azimuth Resolution

The PALSAR was operated at two bandwidths of 14 MHz and 28 MHz. As discussed in Section 2.4, the range resolution is inversely proportional to the radar bandwidth, so the 14 MHz bandwidth has a slant range resolution of 10.8 m and the 28 MHz bandwidth has a resolution of 5.4 m. The azimuth resolution is 1/2 the length of the antenna as discussed in Section 2.4 so all the single look products have an azimuth resolution of 4.5 m, while the ScanSAR products have an azimuth resolution that is 5 times worse (22.5 m).

In the case of ALOS-1 PALSAR, there are 10s of possible configurations, but the mission planners limited the number of modes based on the science needs. Dual and quad polarimetric modes are best for studying ecosystems using temporal

Downloaded from https://www.cambridge.org/core. UNIVERSIDAD AUTONOMA METROPOLITANA, on 11 Nov 2026 at 05:35:40, subject to the Cambridge Core terms of use, available at https://www.cambridge.org/core/terms. https://doi.org/10.1017/9781009606226.009

Table 8.1 *PALSAR imaging characteristics in commonly used modes.*

Mode	Polarization	Band width (MHz)	Look angle (deg)	Range res. (m)	Azimuth res. (m)	B_c (km)	Swath width (km)
FBS	HH or VV	28	8–60 (34.3)	5.4	4.5	13.1	40–70
FBD	HH+HV or VV+VH	14	8–60 (34.3)	10.8	4.5	6.5	40–70
PLR	HH+HV+ VV+VH	14	8–30 (21.5)	10.8	4.5	6.5	20–65
ScanSAR	HH or VV	14 or 28	18–43 (34.3)	5.4 or 10.8	22.5	6.5	350

changes in radar backscatter; interferometry is not usually performed. Interferometry, used for coherence and phase (deformation), has several basic requirements. First, the polarizations of the reference and repeat images must match. There is not much additional information in having more than one polarization, so the fine beam single polarization (FBS) mode is preferred. Second, the reference and repeat swaths must, of course, overlap in the range direction. The radar bandwidths do not need to match, although the lower bandwidth data (14 MHz) must be resampled to match the higher bandwidth (28 Hz). Finally, for ScanSAR, the along-track positions of the bursts must have sufficient overlap to achieve phase coherence. ScanSAR interferometry is discussed in Section 8.4.

8.4 ScanSAR Processing and Interferometry

The first type of wide-swath interferometry is ScanSAR. The systematic observation strategy of ALOS-1 PALSAR provides strip-mode SAR imagery along every ascending orbital track and ScanSAR imagery (Figure 8.4) along every third descending orbital track. Therefore, to obtain a second look direction of PALSAR interferometry sometimes requires processing ScanSAR to ScanSAR mode interferograms. The ScanSAR focusing method used in GMTSAR is based on the proposal by Bamler and Eineder (1996) that, with proper preprocessing, standard strip-mode software (*esarp* in GMTSAR) can be used to construct phase-preserving SAR images and ultimately interferograms. The main advantage of using the standard strip-mode approach, instead of the traditional SPECAN approach (Sack et al., 1985), is that existing and well-tested, strip-mode InSAR processing software can be used. The main disadvantage of this approach is that the zero-padding between the bursts wastes considerable disk space and computer time. Nevertheless, the two approaches should provide equivalent results.

Downloaded from https://www.cambridge.org/core. UNIVERSIDAD AUTONOMA METROPOLITANA, on 11 Nov 2026 at 05:35:40, subject to the Cambridge Core terms of use, available at https://www.cambridge.org/core/terms. https://doi.org/10.1017/9781009606226.009

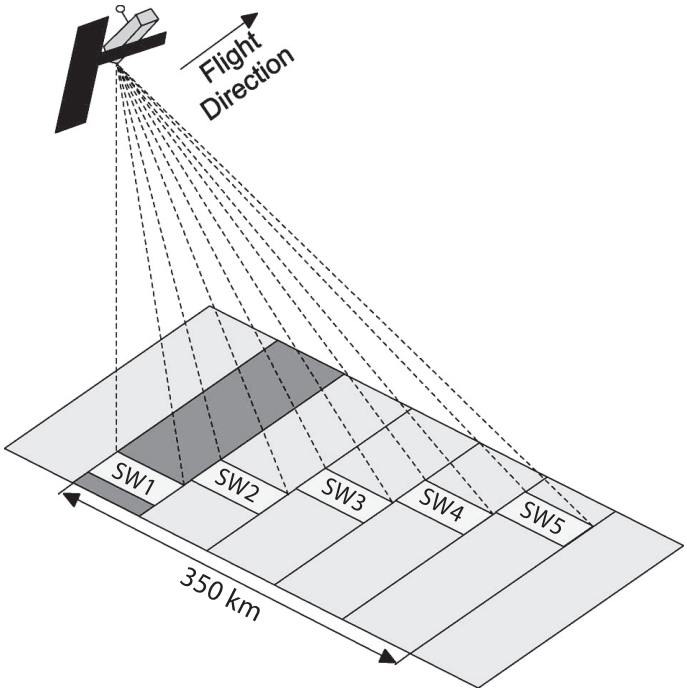


Figure 8.4 Schematic diagram of ScanSAR imaging. The radar acquires data for short bursts over each of 5 subswaths. Each subswath is illuminated over 1/5 of cycle length in the along-track direction such that 4/5 of each subswath is not illumunated. Modified from Bertran-Ortiz and Zebker (2007). Reprinted with permission from *IEEE Transactions on Geoscience and Remote Sensing*.

The GMTSAR ScanSAR mode preprocessor for ALOS was developed and tested using data along a descending orbital track (T538) over Southern California (Tong et al. (2010), Figure 8.3). This track contains two permanently installed radar corner reflectors that are used by JAXA to provide radiometric and geometric calibration for the lifetime of the mission. JAXA has collected PALSAR data over these reflectors in a variety of modes on both ascending and descending tracks. We have extended the ALOS preprocessing software to first perform ScanSAR to FBD mode interferometry and second to perform the more challenging ScanSAR to ScanSAR interferometry where a significant burst overlap is needed. Note that ALOS-2 has the ability to achieve complete burst overlap so this discussion is only relevant to ALOS-1. Indeed, both luck and accuracy are required to achieve a full swath-width ScanSAR to ScanSAR interferogram. The ScanSAR acquisition geometry and parameters for PALSAR are provided in Table 8.2. The five subswaths cover an area 350 km wide. Following Bamler and Eineder (1996), the ScanSAR data are zero-padded to construct strip-mode type data. The original wide

Downloaded from https://www.cambridge.org/core. UNIVERSIDAD AUTONOMA METROPOLITANA, on 11 Nov 2026 at 05:35:40, subject to the Cambridge Core terms of use, available at https://www.cambridge.org/core/terms. https://doi.org/10.1017/9781009606226.009

Table 8.2 *Nominal radar parameters for each subswath. The number of echoes in a burst, nburst, is the only fixed parameter.*

	SW1	SW2	SW3	SW4	SW5
near range (m)	730 097	770 120	806 544	848 515	878 195
PRF *(Hz)*	1 692	2 370	1 715	2 160	1 916
nburst	247	356	274	355	327
$\Delta t(s)$	0.146	0.150	0.160	0.164	0.171
nsamples	4 976	4 720	5 376	4 432	4 688
off nadir (deg)	20.1	26.1	30.6	34.1	36.5

beam (WB1) file contains the bursts of all five subswaths as consecutive rows. The preprocessor separates the data into five separate files where missing lines between the bursts are filled with zeros. Zeros are also added to the end of each echo to match the length of a standard FBD data file. Since the subswaths are processed independently and their amplitude and interferometric phase are recombined in the latitude-longitude coordinate system, an accurate geometric model, precise orbit, and consistent set of processing parameters are required to achieve a seamless recombination. The preprocessing code is rather complex because the pulse repetition frequency (PRF) of the PALSAR echoes varies in three ways. First, as shown in Table 8.2, each subswath has its own PRF optimized to reduce crosstalk. Second, the PRF can change along the satellite track on any one of the subswaths. A PRF change on any subswath changes the time interval and number of zero-pad lines needed on all the other subswaths. Finally, when considering reference and repeat images for interferometry, the PRFs on matching subswaths can be different causing the burst alignment to change along the swath as we find in the example later. In addition, each subswath has its own near range, which varies along the track, so rows must be shifted to align the near range to the common prescribed value. Any small error in the preprocessing could result in a poorly focused image and/or low interferometric coherence.

The first step in the software development was to focus the raw subswath data to form seamless amplitude imagery. We found that the best image quality (i.e., minimal scalloping) was achieved by setting the length of the synthetic aperture to be exactly six bursts. This corresponds to setting the time (~4.7 s) and along-track distance of the synthetic aperture to be exactly the same for each subswath. We also found that by processing the SAR image to zero Doppler, the position of the radar corner reflectors in the image matches the position predicted from the orbit (zero range rate) to within 1 pixel in range and 4 pixels in azimuth. This good match provided confidence that the code is geometrically accurate.

Downloaded from https://www.cambridge.org/core. UNIVERSIDAD AUTONOMA METROPOLITANA, on 11 Nov 2026 at 05:35:40, subject to the Cambridge Core terms of use, available at https://www.cambridge.org/core/terms. https://doi.org/10.1017/9781009606226.009

The second step in the software development was to construct ScanSAR to swath mode interferometry. This combination should always provide interference fringes because there is 100% overlap between the sparse bursts of the ScanSAR and the complete coverage of the swath (Bertran-Ortiz and Zebker, 2007). The ALOS track 538 over Los Angeles has two FBD acquisitions and three ScanSAR WB1 acquisitions. The swath of the FBD data (34.3 incidence angle) overlaps with subswath 4 of the WB1 data. We experimented with three interferometric mode combinations: FBD to FBD, FBD to ScanSAR, and ScanSAR to ScanSAR. The FBD to FBD interferogram had a 10 m baseline and a 46-day timespan, resulting in excellent overall coherence of 0.67. The FBD to ScanSAR interferogram had a somewhat longer baseline of 121 m and a 181-day timespan, resulting in a lower average coherence of 0.38.

The third step in the software development was to construct ScanSAR to ScanSAR interferometry. The major issue here is that there is only a 20% chance of having along- track alignment of the bursts between reference and repeat orbits. There is a question of how much overlap of the bursts is needed to obtain interpretable interference fringes. We were fortunate that two of the ScanSAR images along track 538 have significant burst overlap (up to 78%) and a moderate baseline of 450 m. An interesting aspect of this interferometric pair is that they have different PRFs. This produces a gradual change in burst alignment along the track from 78% at the start of the acquisition to 0% overlap after 18 bursts (Figure 8.5(a)). Phase recovery and coherence (Figure 8.5a, b) are best at the top of the swath and gradually worsen toward the bottom. A plot of row-averaged coherence versus burst overlap fraction (Figure 8.5(c)) illustrates that a maximum coherence of about 0.35 occurs where the burst overlap is greater than 50%. The coherence diminishes to below 0.2 at a burst overlap of 18%. The results show that good interferometric results can be achieved when the burst overlap is greater than about 50%.

8.4.1 M7.8 Gorkha Earthquake Imaged by ALOS-2 ScanSAR InSAR

ALOS-2 was the first L-band satellite to offer burst-aligned ScanSAR interferometry as a standard operating mode. The ScanSAR InSAR capabilities of ALOS-2 proved to be a capable tool for monitoring large continental earthquakes such as the Nepal sequence (Lindsey et al., 2015). The Himalayan region has the largest relief on the Earth, is densely vegetated, and has snow-capped peaks. The L-band radar enables adequate InSAR correlation in the vegetated areas, while tight baseline control of the spacecraft to better than 120 m in these examples (Figure 8.6) minimizes the unwanted phase due to errors in the extreme topography. Finally, the onboard navigation is now accurate enough to provide better than 70% overlap of the ScanSAR bursts between reference and repeat images. This results in

Downloaded from https://www.cambridge.org/core. UNIVERSIDAD AUTONOMA METROPOLITANA, on 11 Nov 2026 at 05:35:40, subject to the Cambridge Core terms of use, available at https://www.cambridge.org/core/terms. https://doi.org/10.1017/9781009606226.009

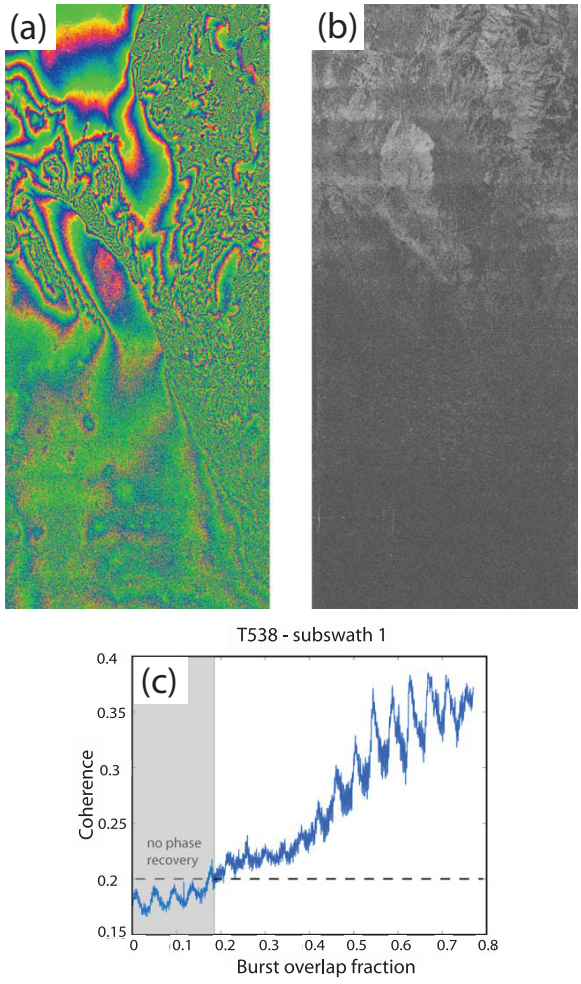


Figure 8.5 ScanSAR to ScanSAR interferogram for subswath 4 of track 538 across the Los Angeles basin. The perpendicular baseline is 450 m and the time interval is 92 days. No topographic phase has been removed. (a) Interferometric phase is high at the top of the swath where burst overlap is large and lower toward the bottom. (b) Coherence also decreases from top to bottom as burst overlap decreases. (c) Row-averaged coherence versus burst overlap.

350 km wide interferograms that can completely image the deformation resulting from these major events. This wide swath also enables a short 14-day repeat interval that enabled the collection of SAR images between the M7.8 and M7.3 events. Slip models based on the deformation spanning the M7.8 event were used to estimate the Coulomb stress that probably triggered the M7.3 event (e.g. Galetzka et al. (2015)). The slip gap observed between the two ruptures (Figure 8.6(b)) can now be monitored for coseismic slip or aseismic creep. The large vertical displacement

Downloaded from https://www.cambridge.org/core. UNIVERSIDAD AUTONOMA METROPOLITANA, on 11 Nov 2026 at 05:35:40, subject to the Cambridge Core terms of use, available at https://www.cambridge.org/core/terms. https://doi.org/10.1017/9781009606226.009

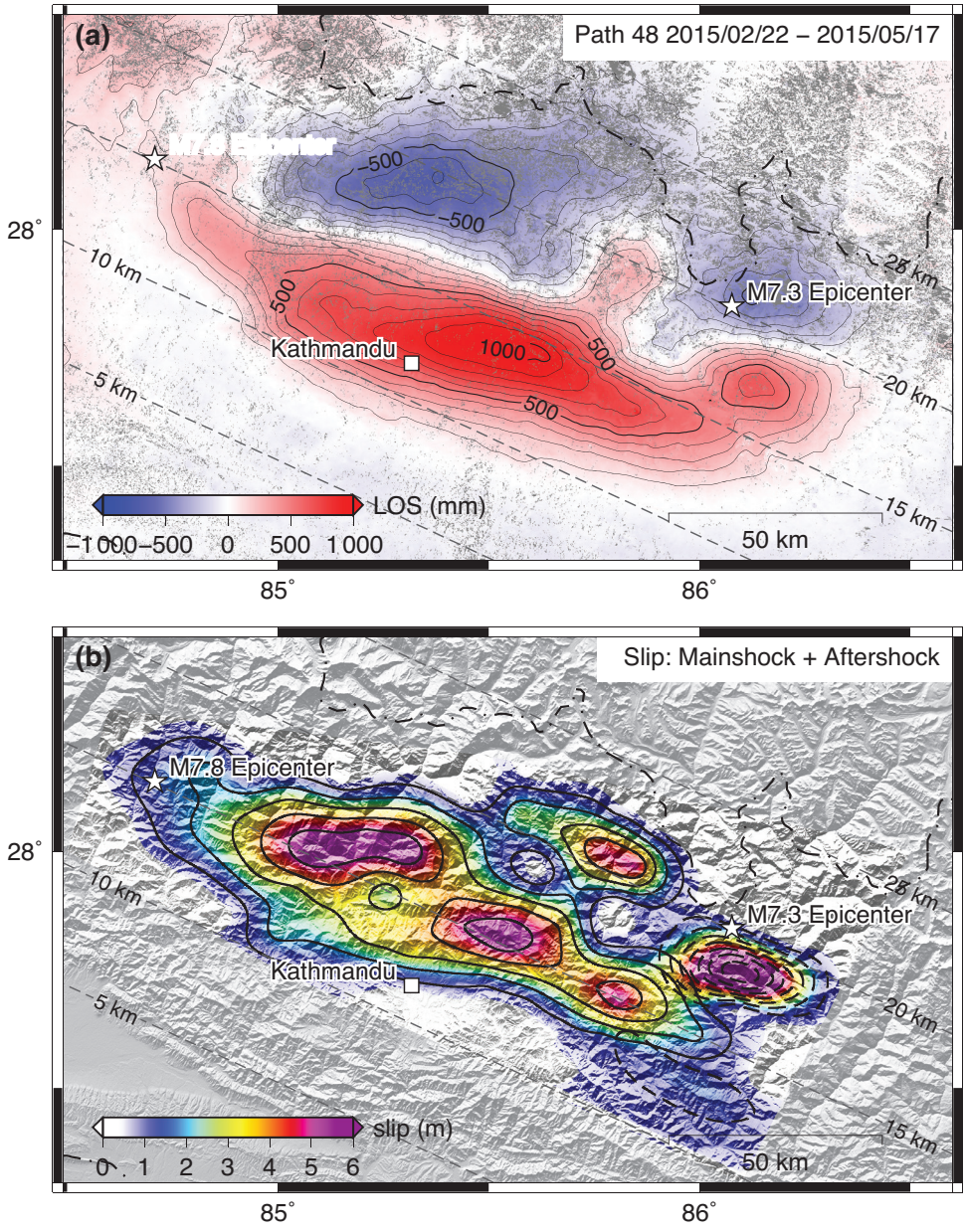


Figure 8.6 (a) Combined surface deformation caused by two major earthquakes in Nepal (M7.8 Gorkha earthquake and a M7.3 aftershock) as measured by the wide swath mode of the ALOS-2 InSAR satellite (Lindsey et al., 2015). The overall extent of the combined rupture is 170 km. This LOS map represents mainly vertical motion with a trough-to-peak amplitude of 1.6 m. (b) Slip inversion based on the modeling approach of Galetzka et al. (2015) shows a peak slip of more than 6 m at a depth of 18 km. The complete InSAR coverage shows that the shallow portion of this megathrust zone remained locked and will slip in the future.

Downloaded from https://www.cambridge.org/core. UNIVERSIDAD AUTONOMA METROPOLITANA, on 11 Nov 2026 at 05:35:40, subject to the Cambridge Core terms of use, available at https://www.cambridge.org/core/terms. https://doi.org/10.1017/9781009606226.009

caused by this thrust event can induce significant viscoelastic deformation over the next years to decades that we hope can be accurately imaged and modeled.

8.5 Terrain Observation by Progressive Scans

8.5.1 Introduction

The second type of wide-swath interferometry discussed in this chapter is Terrain Observation with Progressive Scans (TOPS). The TOPS observation mode is primarily associated with the Sentinel-1 satellites, which are providing regular 6-, 12-, or 24-day acquisitions over all tectonically active land areas. Unlike previous SAR missions, the data from Sentinel-1 are completely open and free through the Copernicus Dataspace Ecosystem (https://dataspace.copernicus.eu/). The short repeat cycle of the satellites was made possible by operating in a burst radar acquisition mode that covers a wide swath of ~230 km. As discussed in Chapter 2, the width of the swath is limited by the length of the antenna and the standard satellites have a maximum swath of ~80 km. One way to increase the swath width is to operate the radar in a ScanSAR mode as described in Section 8.4.1. However, the target may get scattered along azimuth and the amplitude image is subject to modulation or scalloping due to the intermittent radar bursts. A more uniform amplitude is obtained using the TOPS mode (Meta et al., 2010), that electronically steers the antenna from backward looking to forward looking each time a burst acquisition is made within a subswath (Figure 8.7). The steering angle is designed to seamlessly connect the bursts from the same subswath and across the subswaths the continuous coverage is enabled by sufficient overlap from the observations.

While this approach results in a more uniform amplitude radar image, the squint angle is constantly changing, which leads to large variations in the Doppler rate (±2 250 Hz). Traditional radar interferometry is usually performed using data close to zero Doppler or at a Doppler that is much smaller than the PRF. Indeed, to achieve phase coherence of the interferogram, the Doppler centroids of the reference and repeat image must overlap by at least 20% as described in Section 8.4.1. Data acquired in the TOPS mode sweeps over nine PRF intervals during one scan as shown in Figure 8.8(a). Thus, any resampling of the radar images requires deramping the data first. Then one can perform regular operations on the data and restore the ramping function afterward.

Another problem caused by the antenna steering is that it dramatically increased the phase sensitivity to azimuthal misregistration at burst boundaries. Typically, the small misregistrations are likely from the slight difference in the orbital velocity, or burst timing of the reference and repeat acquisitions. However, due to the large difference between the Doppler at the upper and lower edge of each burst ($f_u - f_l$), a small azimuthal misregistration will result in a significant phase difference. Indeed

Downloaded from https://www.cambridge.org/core. UNIVERSIDAD AUTONOMA METROPOLITANA, on 11 Nov 2026 at 05:35:40, subject to the Cambridge Core terms of use, available at https://www.cambridge.org/core/terms. https://doi.org/10.1017/9781009606226.009

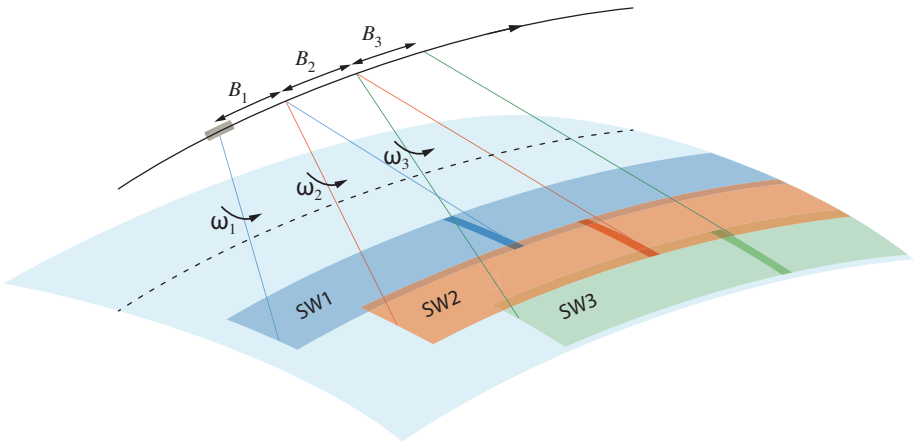


Figure 8.7 Diagram of the TOPS acquisition geometry where v is the velocity of the satellite, B is the burst duration, and ω is the steering rate. Each subswath is about 80 km wide and each burst covers a 20 km distance in the along-track direction (Mittermayer et al., 2010). There is some overlap between the subswaths and bursts to provide a seamless mosaic of amplitude and phase. The phase difference in the overlap areas can be used to refine the image alignment. This is called *enhanced spectral diversity*.

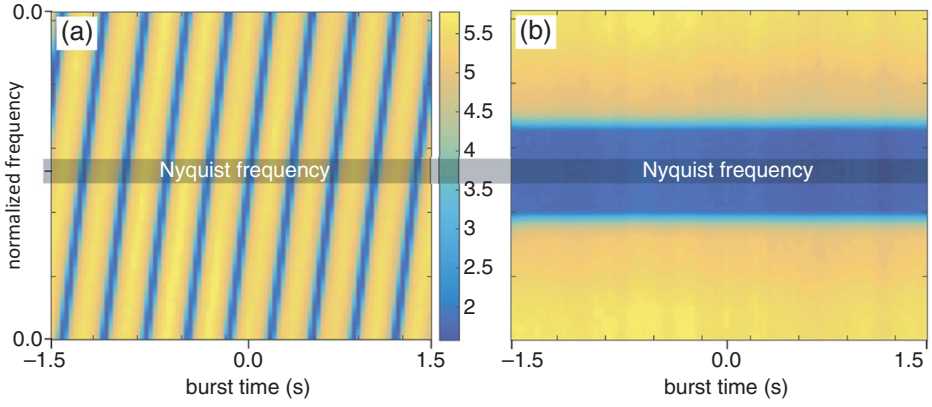


Figure 8.8 Spectrogram of one burst of TOPS-mode data plotted on a log color scale. (a) Original spectrogram of a single burst of TOPS data wraps around the Nyquist frequency nine times. (b) Spectrogram after deramping has low power close to the Nyquist, which enables accurate resampling.

one can use the phase difference ϕ in the small burst overlap areas to estimate the azimuth shift Δa needed to reduce this phase mismatch

$$\Delta a = \mathrm{PRF}\frac{\phi}{2\pi\left(f_u - f_l\right)} \tag{8.1}$$

Downloaded from https://www.cambridge.org/core. UNIVERSIDAD AUTONOMA METROPOLITANA, on 11 Nov 2026 at 05:35:40, subject to the Cambridge Core terms of use, available at https://www.cambridge.org/core/terms. https://doi.org/10.1017/9781009606226.009

For S1A, the top-to-bottom Doppler difference is 4 500 Hz and the effective PRF is 486 Hz. Keeping the phase mismatch below 0.54 radian (2.8 mm), for example, requires azimuth alignment to 0.01 pixel accuracy. This method is called *enhanced spectral diversity* and the implementation is discussed further in Section 8.5.4.

8.5.2 Traditional Image Alignment Fails with TOPS-Mode Data

The traditional approach to InSAR image alignment is done in three steps: (1) First, the orbital information is used to make a rough (1-2 pixel accuracy) estimate of the offset of the reference and secondary images. (2) Then 2-D cross-correlation of sub-patches of data (e.g., 64 by 64 pixels) is used to estimate the affine transformations (Equation 8.2) needed to map the secondary image onto the reference image. As described in Chapter 3, the trajectories of the reference and secondary images are very smooth so their differences in both the range dr and azimuth da coordinates are well described by the following equations

$$\begin{aligned} dr &= c_0 + c_1 r_m + c_2 a_m \\ da &= c_3 + c_4 r_m + c_5 a_m \end{aligned} \tag{8.2}$$

where r_m and a_m are the range and azimuth coordinates of the reference image and there are six unknown coefficients c_0 to c_5. The coefficients are determined by fitting planes to the range and azimuth offset data derived from the cross-correlation of the sub-patches. It seems reasonable that six parameters are sufficient to account for the orbital differences because the orbit is well described by a six-element state vector, and the differences in the reference and secondary state vectors are very small over the time span of the radar acquisition. (3) The final step is to use a 2-D sinc-function interpolator to resample the secondary image into the coordinates of the reference image (*resamp* in GMTSAR). The accuracy of the alignment depends on the coherence between the reference and repeat images. When coherence is high, the two images can be aligned to 0.1 pixel accuracy. When the coherence is low, the alignment can be worse than 1.0 pixel. The method fails when the reference and secondary images have poor correlation.

This standard approach to image alignment works well on swath-mode SAR data as well as ScanSAR data; however, it fails with the TOPS-mode data for two reasons. First, the traditional method can only achieve 0.1 pixel alignment accuracy, but as discussed earlier, the alignment must be better than 0.01 pixel to keep the phase mismatch between the burst boundaries below 2.8 mm. Second, because the azimuth spectrum of the TOPS-mode data has frequencies well above the Nyquist sampling frequency of the single look complex (SLC) data (Figure 8.8(a)), the standard sinc-function interpolation fails.

Downloaded from https://www.cambridge.org/core. UNIVERSIDAD AUTONOMA METROPOLITANA, on 11 Nov 2026 at 05:35:40, subject to the Cambridge Core terms of use, available at https://www.cambridge.org/core/terms. https://doi.org/10.1017/9781009606226.009

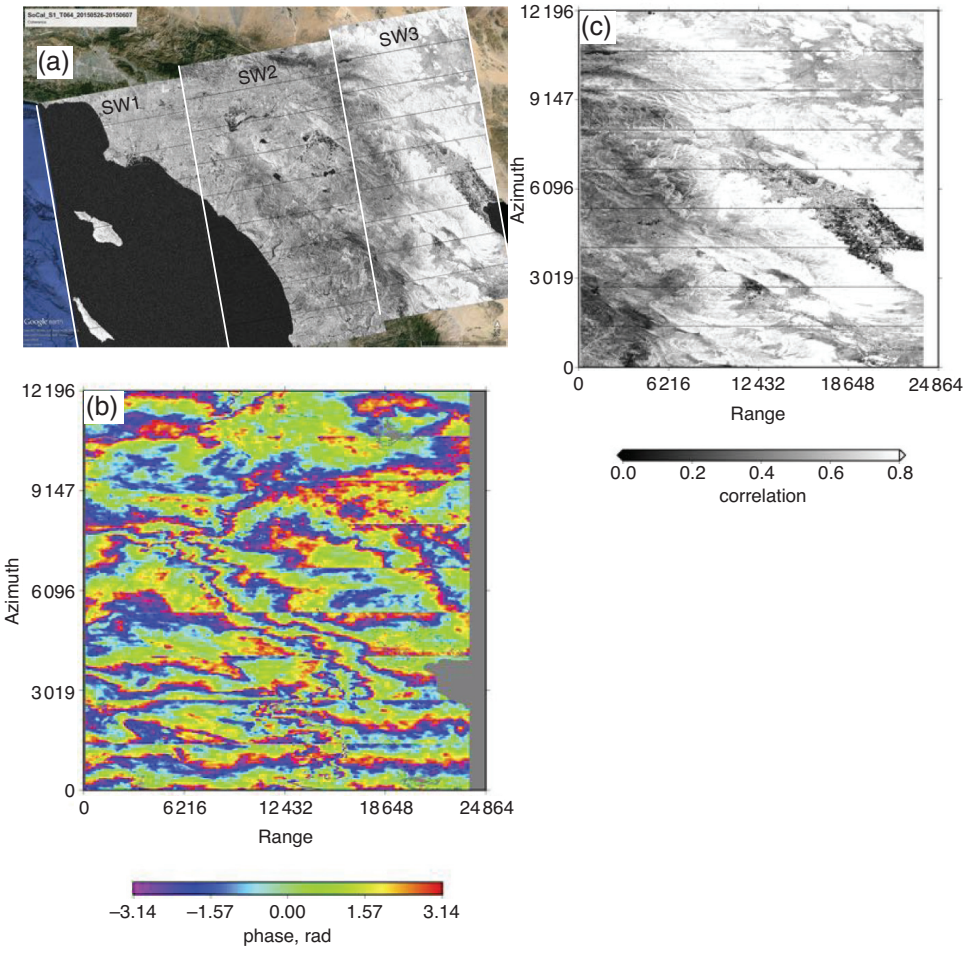


Figure 8.9 (a) Coherence image of test area for track 064 dates 20150526 and 20150607. The S1A data have three subswaths with nine bursts each. (b) InSAR phase of subswath 3 in radar coordinates shows phase mismatch at burst boundaries as well as banding within each burst. (c) InSAR coherence is generally high with eight lines of low coherence due to the phase mismatch as well as banding within each burst due to poor performance of the sinc interpolator across the Nyquist frequency.

An example interferogram of using this traditional approach to align a reference and secondary SLC image of S1A TOPS mode is shown in Figure 8.9. There are two main problems that need to be corrected. The first is that there are large phase mismatches at the eight boundaries between the nine bursts. Second, because the azimuth spectrum of the TOPS-mode data has Doppler far beyond the Nyquist frequency of the SLC data (Figure 8.8(a)), the standard sinc-function interpolation will introduce aliasing to the resampled data.

Downloaded from https://www.cambridge.org/core. UNIVERSIDAD AUTONOMA METROPOLITANA, on 11 Nov 2026 at 05:35:40, subject to the Cambridge Core terms of use, available at https://www.cambridge.org/core/terms. https://doi.org/10.1017/9781009606226.009

8.5.3 Geometric Alignment Approach

Overcoming these two issues requires two new approaches: geometric alignment based on a precise orbit (Sansosti et al., 2006) and deramping of the SLC data prior to interpolation. The Sentinel-1 SAR data are provided with a high-accuracy orbit (~2–3 cm radial and cross track, ~5 cm along-track (Fernandez et al., 2015) available at https://dataspace.copernicus.eu/). This high accuracy in orbital determination enables purely geometric registration to remove almost all the phase mismatch at the burst boundaries. The underlying idea is to calculate the exact radar coordinates for the same set of terrain points utilizing information from the precise reference and secondary orbits. The differences between the coordinates reflect the needed shifts to perform coregistration.

The algorithm for deramping the secondary image prior to interpolation is described in the ESA documentation (Miranda, 2015), and all the parameters are provided with the metadata that accompany the SAR imagery files. The ramps are restored to each burst after resampling, thus any possible inaccuracies in the de-ramping function will introduce no error to the radar phase. Best results are achieved if the de-ramping and re-ramping are only performed on secondary images, leaving the master image unchanged. De-ramping, interpolation, and re-ramping are performed burst by burst, after which all bursts within one subswath are stitched together to generate one SLC image. Compared to the traditional cross-correlation method, this geometric approach could essentially apply coregistration pixel by pixel instead of fitting the affine transformation parameters (Table 8.3).

The overall algorithm for coregistering the TOPS-mode Sentinel-1 data (Figure 8.10) can be summarized as follows:

1. Construct a low-resolution (~12 arc-seconds) digital elevation model covering the area of the SLC images. If no elevation data are available (e.g., Antarctica), a guess at the mean elevation can help with coregistration.

Table 8.3 *Example of precisely estimated range (r_m) and azimuth (a_m) along with range change (dr) and azimuth change (da) from master image to secondary image.*

r_m	dr	a_m	da
21612.658170	68.048382	9.502554	5.581971
21545.310230	68.050767	5.672641	5.582379
21476.796745	68.049944	1.840498	5.582791
21589.753434	68.052334	35.595495	5.582574
21522.753310	68.054712	31.765366	5.582985
21454.950368	68.057071	24.101007	5.583396
21386.133332	68.059421	16.432719	5.583806

Downloaded from https://www.cambridge.org/core. UNIVERSIDAD AUTONOMA METROPOLITANA, on 11 Nov 2026 at 05:35:40, subject to the Cambridge Core terms of use, available at https://www.cambridge.org/core/terms. https://doi.org/10.1017/9781009606226.009

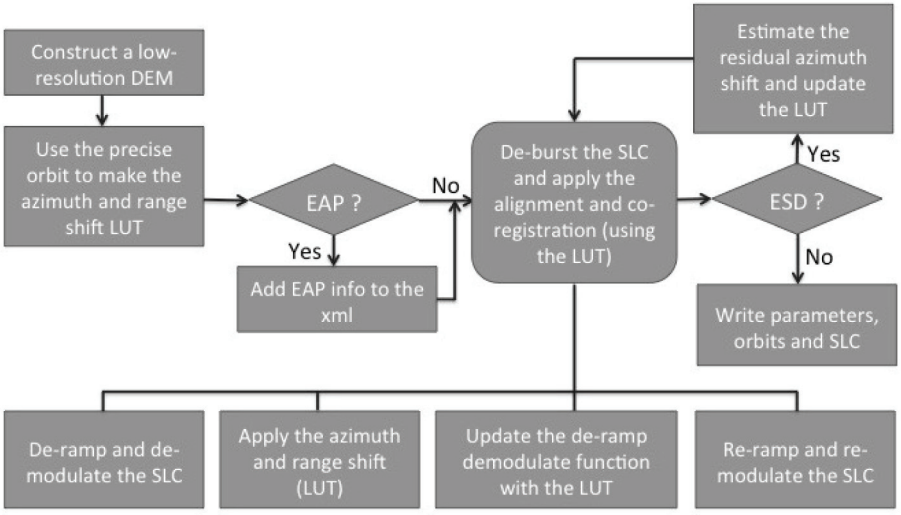


Figure 8.10 Preprocessing chain for TOPS data using precise orbits and point-by-point geometric coregistration. In the flowchart, LUT denotes look-up table, EAP is short for elevation antenna pattern correction, which is only needed for SLC data processed with early Instrument Processing Facility (IPF) version. ESD is short for enhanced spectral diversity.

2. Use the precise orbital information to map each pixel of longitude, latitude, and height into the range and azimuth of the radar pixel coordinates. This is done as described in Section 3.7 where one finds the azimuth of the closest range (i.e., zero Doppler) on the orbital trajectory to each topography pixel – first using a golden section search algorithm and then performing a polynomial refinement. Step 2 is done for both the master and secondary images.
3. Construct two tables (i.e., grids) of range (azimuth) difference, secondary minus master, versus range and azimuth. An example is provided in Table 8.3. These grids provide a mapping of the secondary image onto the master image. This mapping is then used for pixel-by-pixel coregistration. An alternative approach is to estimate the six-parameter affine transformation described in Equation 8.2.
4. Deburst the master image to make a continuous SLC. This is done by calculating the boundaries between bursts using the azimuth time for each line in the burst and eliminating overlapping lines. Stitching of the bursts is done using the center of the overlapped area between bursts.
5. Read a burst of secondary SLC data, compute the deramp-demodulating function following the ESA documentation (Miranda, 2015), and apply the deramp-demodulation function to the SLC data to remove the ramp induced by the antenna steering. An example of a deramped spectrum for a burst is shown in Figure 8.8(b). This removal enables proper resampling of the secondary image.

Downloaded from https://www.cambridge.org/core. UNIVERSIDAD AUTONOMA METROPOLITANA, on 11 Nov 2026 at 05:35:40, subject to the Cambridge Core terms of use, available at https://www.cambridge.org/core/terms. https://doi.org/10.1017/9781009606226.009

6. Use a 2-D sinc function to interpolate the fractional part of the range and azimuth shift of the secondary SLC into the coordinates of the master image, using grids of offsets created from the look-up table developed in step 3.
7. Recompute the deramp-demodulate function applying the same range and azimuth offsets and output the coregistered burst of the secondary SLC data.
8. Repeat steps 5–7 until all bursts of the secondary SLC from the same subswath are coregistered. Deburst the secondary SLC and stitch at the center of the overlapped area between bursts.
9. If the alignment requires further coregistration using enhanced spectral diversity, steps 4–8 are replaced with outputting the overlapped area between the bursts, that is, forward-looking SLCs (SLCH) and backward-looking SLCs (SLCL). They are used to compute double-difference interferograms and estimate residual shifts needed to update the offset maps in step 3. Then perform regular coregistration as from step 4 to step 8.

   At this point, we have master and secondary SLCs that are coregistered to the accuracy of the orbit data. Note that this accuracy is far better than 0.1 pixel so the interferometric coherence between the reference and secondary should be optimal, assuming no range/azimuth shifts due to changes in the atmosphere and ionosphere between the reference and secondary imaging times. An example of the geometrically aligned interferogram for the same data as shown in Figure 8.9(b,c) is shown in Figure 8.11. Note the loss of coherence near burst boundaries is due to the sharp Doppler change. A remarkable result of this geometric alignment approach is that one can align many secondaries to a single master so after this alignment, any two of the secondary images can be used to form highly coherent interferograms. This greatly improves processing efficiency for large stacks of Sentinel-1 InSAR data.

8.5.4 Enhanced Spectral Diversity

In a few cases, the along-track orbit error (or time tag error) may result in an interferogram having an unacceptable phase mismatch at the burst boundaries. Along-track mismatch can also occur if there is motion of the surface between the reference and repeat images perhaps due to motion of the tectonic plate or ice relative to the orbit reference frame. If there is adequate coherence between the reference and repeat SAR images, the phase mismatch can be used to estimate the azimuth shift of the repeat image (Prats-Iraola et al., 2012). The phase difference ϕ in the overlap zones can be extracted from a double-difference interferogram.

$$s_{sd} = \left(s_{u,m} \cdot s_{u,s}^{*}\right) \cdot \left(s_{l,m} \cdot s_{l,s}^{*}\right)^{*} \tag{8.3}$$

$$\phi = \arg\left(s_{sd}\right) \tag{8.4}$$

Downloaded from https://www.cambridge.org/core. UNIVERSIDAD AUTONOMA METROPOLITANA, on 11 Nov 2026 at 05:35:40, subject to the Cambridge Core terms of use, available at https://www.cambridge.org/core/terms. https://doi.org/10.1017/9781009606226.009

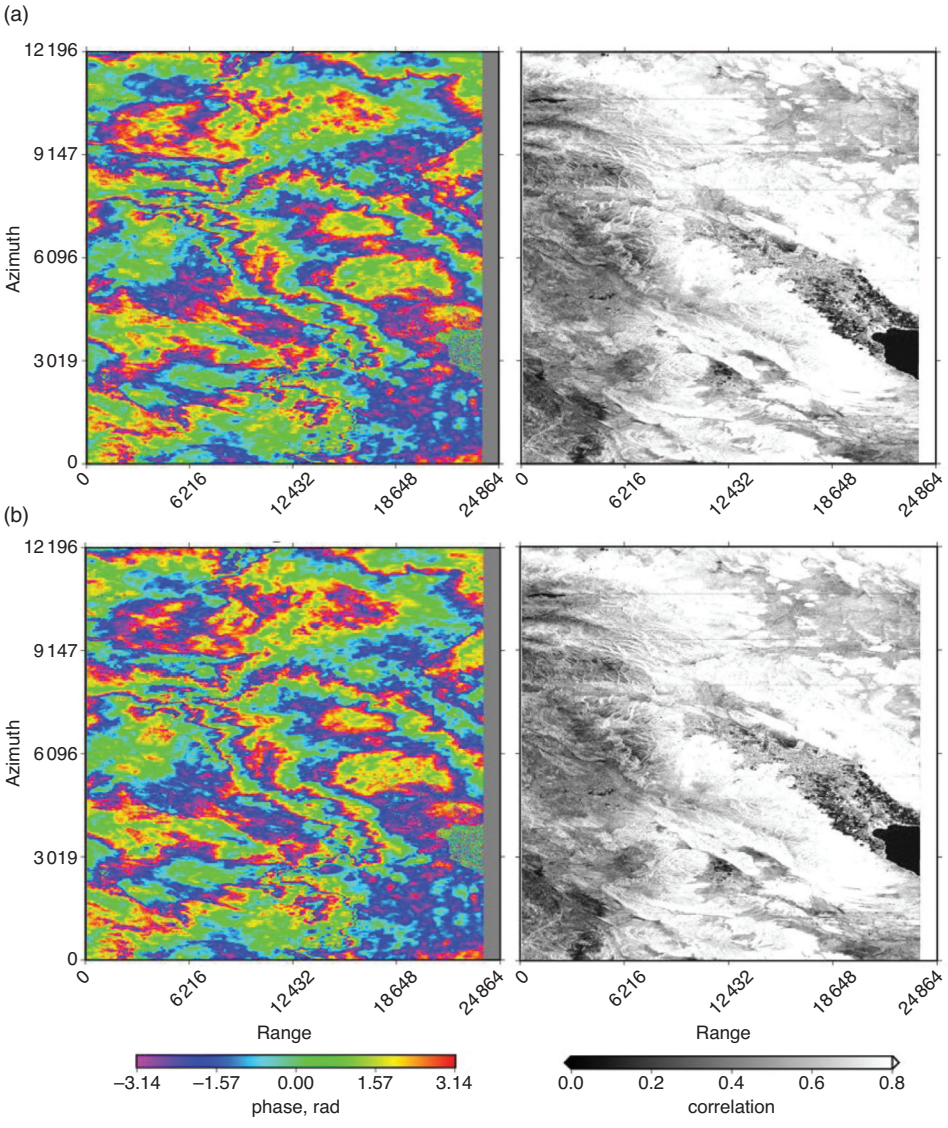


Figure 8.11 Interferogram and coherence of SW3 of the Southern California pair (20150526-20150607) processed with alignment/registration by six-parameter affine transformation (a) and point-by-point (b). The phase mismatch at burst boundaries is no longer visible. There is a slightly lower correlation at the burst boundaries reflecting a subtle phase offset. The differences between the six-par method and the PBP method are very small except in cases of long InSAR baseline and high-amplitude topography.

Downloaded from https://www.cambridge.org/core. UNIVERSIDAD AUTONOMA METROPOLITANA, on 11 Nov 2026 at 05:35:40, subject to the Cambridge Core terms of use, available at https://www.cambridge.org/core/terms. https://doi.org/10.1017/9781009606226.009

where, for example, $s_{u,m}$ is the SLC of the upper portion of the overlap zone for the master. In practice, one computes and filters double-difference interferograms for all the pixels in multiple overlap zones. Then the median phase from all the pixels is used in Equation 8.1 to calculate a single residual azimuth shift to update the azimuth shift *da* in Table 8.3. In some extreme cases, there is a bivariate residual azimuthal shift, likely due to strong perturbation from the ionosphere; one could use an additional range-dependent, azimuth shift parameter to account for the spatial variation (Wang et al., 2017). The major problem with ESD is that it requires adequate coherence between every secondary image and the master image, though one can improve the ESD accuracy by forming a network of estimates, thus mitigating the effect from loss of coherence (Fattahi et al., 2017). Another problem with enhanced spectral diversity (ESD) is that it absorbs all components that cause phase discontinuities and treats them as misregistration. In reality, actual ground deformation in the azimuthal direction could cause discontinuities between bursts, either from earthquakes (Grandin et al., 2016) or tectonic motion (Yague-Martinez and Prats-Iraola, 2022). In such a scenario, they should not be treated as misregistration errors, but as useful signals. We will discuss this approach of burst overlap interferometry (BOI) in Chapter 10.

8.6 SweepSAR

The third type of wide-swath interferometry discussed in this chapter is SweepSAR (Freeman et al., 2009). The ScanSAR and TOPS-mode radars achieve a wider swath by subsampling the along-track illumination of the Earth. For example, the ScanSAR-mode of the ALOS-1/2 radars achieves a 350 km wide swath using five subswaths and samples these subswaths only 1/5 of the time (Figure 8.4). Similarly, the TOPS mode has three subswaths and the radar under-samples the Doppler spectrum by a factor of 3 in the along-track direction to achieve a 250 km wide swath (Figure 8.7). These approaches have fewer looks per surface area than the strip-mode approach, so the data are noisier in both amplitude and phase.

An alternate approach that achieves a 240 km wide swath and also has the full resolution of a strip-mode SAR has been proposed by Freeman et al. (2009) and will be implemented in the upcoming (expected launch in 2025) NISAR mission (Rosen et al., 2017). This is called SweepSAR and it uses a large reflector antenna (12 m in diameter) combined with a phased array, scan-on-receive, to enable a 240 km wide swath at full resolution (Figure 8.12). On transmit, the radar illuminates the full 240 km-wide swath. To achieve full along-track resolution, the inter-pulse interval 1/PRF is shorter than the time it takes for the pulse to sweep from the near-range to the farrange. To avoid overlap of the pulses in time, the receive array can focus narrowly in the cross-track direction. A very simplified schematic of how

Downloaded from https://www.cambridge.org/core. UNIVERSIDAD AUTONOMA METROPOLITANA, on 11 Nov 2026 at 05:35:40, subject to the Cambridge Core terms of use, available at https://www.cambridge.org/core/terms. https://doi.org/10.1017/9781009606226.009

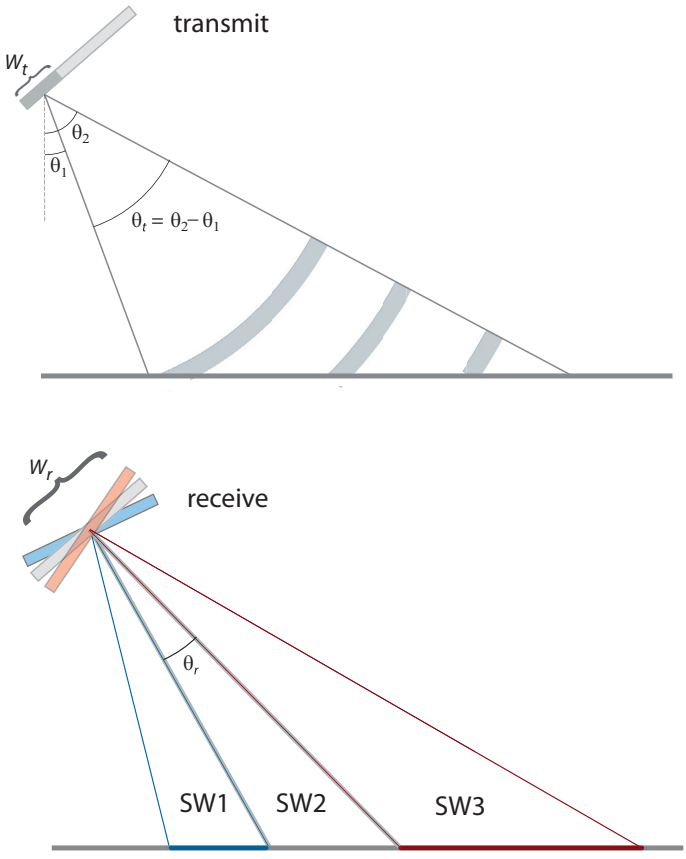


Figure 8.12 Highly schematic diagram looking along the flight direction of the spacecraft of the SweepSAR method. The full width of the antenna (or reflector in the case of NISAR) is W_r. On transmit, a fraction of that width W_t is used to create a relatively wide beam angle θ_t thus illuminating a wide swath. On receive, the full antenna width is used W_r to create a relatively narrow beam angle θ_r that records only the reflections over a narrow subswath (SW1, 2, or 3). The antenna is not actually turned to change the receive beam position; this is performed using a phase array. Note that a reflector is used on NISAR. When the pulse is transmitted, all the T-modules can be used for maximum power and maximum SNR. The wide transmit array creates a narrow beam on the reflector W_t, resulting in a relatively wide beam angle to illuminate the wide swath. Similarly, on receive, a fraction of the R-modules are used that have a broader angular aperture in the reflector, which results in a narrower beam on the ground.

this is achieved is shown in Figure 8.12. In this schematic modified from Freeman et al. (2009), the planar antenna has a width W_r, that is similar to the length of a normal SAR antenna L (12 m). Full swath illumination in the cross-track direction is achieved by using a fraction of the full antenna width W_t. From the analysis in

Downloaded from https://www.cambridge.org/core. UNIVERSIDAD AUTONOMA METROPOLITANA, on 11 Nov 2026 at 05:35:40, subject to the Cambridge Core terms of use, available at https://www.cambridge.org/core/terms. https://doi.org/10.1017/9781009606226.009

Chapter 2, $\sin\theta_t = \lambda/W_t$, so a smaller width, smaller than a normal strip-mode SAR, is needed to achieve a larger projection angle to illuminate the 240 km wide swath.

To avoid aliasing of the return pulses that are simultaneously reflected from the near, center, and far ranges, the full width of the antenna is used to divide the return energy into multiple beams (Figure 8.12). Beam 1 tracks the pulse over the subswath 1 (SW1), but the energy of this pulse will be outside beam 1 when it propagates to SW2 and SW3. Beam 2 tracks the pulse when it enters SW2 and beam 3 tracks the pulse when it enters SW3. This is a greatly simplified description of the SweepSAR method, but it illustrates some of the basic physics. NISAR has a 12 m diameter reflector that serves as the large planar antenna shown in Figure 8.12 and the transmit and receive arrays are located on the body of the spacecraft 9 meters below the reflector. The overall result of this marvel of engineering is a full-resolution strip-mode SAR that can achieve a wide swath. The 240 km wide swath can completely cover the Earth at the equator in 177 orbits, which corresponds to a 12-day repeat cycle. A standard strip-mode SAR has a repeat cycle 3–4 times longer.

8.7 Problems

1. ScanSAR is a technique to construct a very wide swath radar image by emitting a burst of ~300 radar pulses on a narrow subswath and systematically cycling the near range of each burst to illuminate five parallel subswaths ultimately forming a wide swath. Why is it not possible to simply illuminate the wide swath with continuous wide pulses? Hint: see Equation 2.16.
2. How can a standard strip-mode SAR processor be used to focus ScanSAR data? What are the advantages and disadvantages of this approach?
3. Phase coherence for regular swath-mode interferometry is only possible when the baseline between the reference and repeat images is less than the critical baseline and there is significant overlap in the Doppler spectra of the reference and repeat images. What additional attribute is needed to achieve phase coherence for ScanSAR interferometry?
4. How many different interferometric combinations are possible for 10 SAR images? For 100 SAR images? For n SAR images?
5. Derive Equation (8.1).
6. Give two reasons why the standard cross-correlation imaging matching approach is not adequate for TOPS-mode data?
7. Why must the bursts be deramped prior to sinc interpolation?
8. Why does a six-parameter affine transformation model work well when the interferometric baseline is small and the topography has low relief?

Downloaded from https://www.cambridge.org/core. UNIVERSIDAD AUTONOMA METROPOLITANA, on 11 Nov 2026 at 05:35:40, subject to the Cambridge Core terms of use, available at https://www.cambridge.org/core/terms. https://doi.org/10.1017/9781009606226.009